Chronoamperometry and Cyclic Voltammetry at Conical Electrodes, Microelectrodes, and Electrode Arrays: Theory

Edmund J. F. Dickinson, Ian Streeter, and Richard G. Compton*

Physical and Theoretical Chemistry Laboratory, Oxford University, South Parks Road, Oxford, United Kingdom OX1 3QZ

Received: December 20, 2007; In Final Form: January 9, 2008

The finite difference method is used to simulate chronoamperometry, linear sweep voltammetry, and cyclic voltammetry at conical electrodes and microelectrodes. Techniques for the numerical simulation of these processes at microdiscs are adapted and extended to accurately model diffusion to the electroactive cone surface. Simulated results are analyzed, and trends are rationalized in terms of the cone apex angle, α. The diffusion domain approximation is used to extend the theory to regular and random arrays of conical electrodes.

1. Introduction

The geometry of an electrode dictates the nature of mass transport to its surface, and so relates closely to its behavior when employed in diffusionally dependent analytical techniques such as chronoamperometry or voltammetry. New lithographic techniques[1−5] permit the manufacture of electrodes and arrays of electrodes with precisely defined geometry, at the micro- or nanoscale. Although the properties of microelectrode arrays have been well characterized for simple geometries,[6,7] more complicated geometries, which may offer increased current density or improved resolution of electrochemical mechanisms, have not been extensively studied. Accordingly, we are presently researching the electrochemical responses at improved and enhanced electrode shapes and geometries, via computer-aided simulation.

This paper sets out the theory for simulating electrodes with conical geometry, and briefly summarizes its execution through numerical methods. Diffusion-limited steady-state currents for an isolated conical electrode are assessed and compared with values reported in previous work.[8] The theory is then expanded beyond previous study to discuss chronoamperometry, linear sweep voltammetry, and cyclic voltammetry at isolated conical electrodes. Finally, the diffusion domain approximation[9] is applied to discuss regular and random arrays of conical electrodes, as might feasibly be used in an experimental situation. Comparison is drawn throughout with the well-established behavior of microdisc electrodes, in order to assess the comparative utility of the conical geometry.

2. Theory for Simulating Conical Electrodes

2.1. Geometry of a Cone. A cone is defined geometrically by two parameters: its basal radius r, and the angle between its axis and its surface, α. Cones, like discs, are axisymmetric, so an (r,z) cylindrical coordinate system is appropriate for study. This is normalized to the basal radius of the electrode, r_e, to generate dimensionless (R,Z) as follows:

$$R = r/r_e; \quad Z = z/r_e \qquad (1)$$

A diagram of a generic cone is presented at Figure 1. It follows directly that

$$\tan \alpha = \frac{1}{Z_e} \quad \text{so} \quad Z_e = \cot \alpha \qquad (2)$$

and that the electroactive surface area is

$$A_{cone} = \pi\sqrt{1 + Z_e{}^2} = \pi\sqrt{1 + \cot^2 \alpha} \qquad (3)$$

In the same coordinate system, $A_{disc} = \pi$, so a suitable dimensionless area is

$$A_{dim} = \frac{A_{cone}}{A_{disc}} = \sqrt{1 + \cot^2 \alpha} \qquad (4)$$

2.2. Simulation Procedure. A simple one-electron oxidation of the form

$$A \rightleftharpoons B + e^- \qquad (5)$$

is assumed throughout. The system is modeled by solving Fick's second law of diffusion, which, in an appropriate system of dimensionless coordinates (see Table 1), and with equal diffusion coefficients for A and B, reduces to

$$\frac{\partial a}{\partial T} = \frac{\partial^2 a}{\partial Z^2} + \frac{1}{R}\frac{\partial a}{\partial R} + \frac{\partial^2 a}{\partial R^2} \qquad (6)$$

This is solved by discretization in (R,Z) to an appropriate 2D grid of points over the simulation space. A resulting series of coupled simultaneous equations is generated using an alternating direction implicit (ADI) finite difference method,[10] and solved using a generalized Thomas (tridiagonal matrix) algorithm,[11] implemented in C++.

The equation is solved at successive timesteps, with boundary conditions evolving in T as appropriate. For studies of cyclic voltammetry and the chronoamperometric transient, regular timesteps were used. For $T \rightarrow \infty$ studies of steady-state currents, an expanding time grid was used, with timesteps expanding as $T^{1/2}$. In all cases, the density of timesteps was sufficient to render negligible any oscillations resulting from the $T = 0$ singularity in the region of interest.

* Corresponding author. Fax: +44 (0) 1865 275410. Tel: +44 (0) 1865 275413. E-mail: richard.compton@chem.ox.ac.uk.
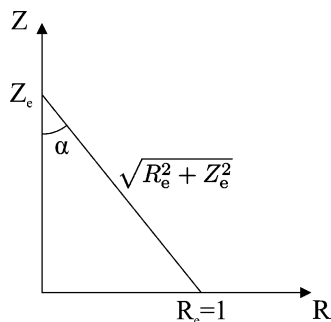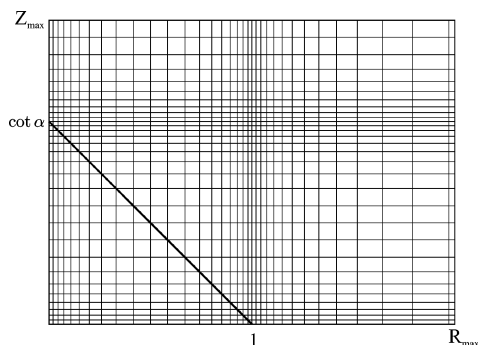
4060 *J. Phys. Chem. B, Vol. 112, No. 13, 2008*

Dickinson et al.

Figure 1. Cross-section of a cone in (R, Z).

Figure 2. Expanding grid of points used in this work (some lines excluded for clarity).

TABLE 1: Dimensionless Parameters Used in Numerical Simulations Where c_A and c_B are the Concentrations of A and B, Respectively, and k^0 is the Heterogeneous Rate Constant for Electron Transfer

parameter	definition
R	r/r_e
Z	z/r_e
A_{dim}	$\sqrt{1 + \cot^2 \alpha}$
T	$D_A t/r_e^2$
θ	$(F/RT)(E - E_f)$
σ	$(r_e^2/D_A)(F/RT)v$
a	$c_A/c_{A,bulk}$
b	$c_B/c_{A,bulk}$
j	$i/FD_A c_{A,bulk} r_e 2\pi$
K^0	$k^0 r_e/D_A$

Efficient constructions for grids that minimize computational time while retaining accuracy are well documented for microdiscs.[12] In the microdisc case, the highest density of points is required close to the electroactive surface at $Z = 0$, and close to the electrode−insulator boundary at $R = 1$. The approach to cones must differ from discs, as the electroactive surface is not confined to $Z = 0$, nor is it parallel to the R coordinate. There is also a singularity at the cone apex, $Z = Z_e$, in addition to that at the cone edge, $R = 1$.

The expanding grid used in this work is adapted from the related microdisc grid by expanding exponentially from the electrode−insulator boundary in *both* dimensions (see Figure 2). There is then a high density of points close to all singularities, as shown. We note that a similar grid was employed independently, with the same concerns in mind, by Britz et al. in their study of conical wells.[13] Grid points are fitted precisely to the sloping surface of the cone by scaling grid spacings in the Z direction by $\cot \alpha$ vs those in the R direction, i.e.,

$$R_{i+1} - R_i = h_i; \quad Z_{i+1} - Z_i = k_i \qquad (7)$$

$$k_i = h_i \cot \alpha \qquad (8)$$
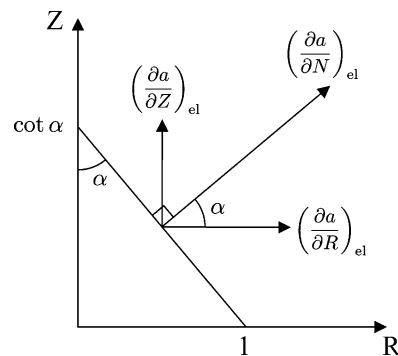
Figure 3. The normal coordinate N.

2.3. General Boundary Conditions. For the simple case of equal diffusion coefficients, $D_A = D_B$, the extent of the diffusion layer will not exceed $6\sqrt{T}$ from the electrode surface;[14] simulation further from the electrode has no effect on observed current. For an isolated cone, the simulation space is therefore appropriately bounded by

$$R_{max} = 1 + 6\sqrt{T_{max}}; \quad Z_{max} = \cot \alpha + 6\sqrt{T_{max}} \qquad (9)$$

A bulk boundary condition is set at these limits; concentration is set to zero within the bounds of the cone. At $R = 0$ and $Z = 0$ in the insulating region, a zero-flux boundary condition is set.

$$Z = Z_{max}, R = R_{max}; \quad a = 1, \ b = 0 \qquad (10)$$

$$R < 1, Z < (1 - R) \cot \alpha; \quad a = b = 0 \qquad (11)$$

$$Z = 0, R > 1; \quad \frac{\partial a}{\partial Z} = \frac{\partial b}{\partial Z} = 0 \qquad (12)$$

$$R = 0, Z > \cot \alpha; \quad \frac{\partial a}{\partial R} = \frac{\partial b}{\partial R} = 0 \qquad (13)$$

Electrochemical boundary conditions are set at the electrode, and are dependent on the process simulated. To simulate mass-transport limited current, the condition $a_{el} = 0$ is used. The $(1/R)$ term in Fick's second law is eliminated at the boundary $R = 0$ using a Maclaurin expansion, as reported by Gavaghan.[15]

2.4. Boundary Conditions and Flux Calculation Normal to the Surface. Butler−Volmer boundary conditions must be set in a coordinate normal to the electroactive surface, defined as N (see Figure 3). The flux at the electroactive surface is then specified in this direction, such that

$$\left(\frac{\partial a}{\partial N}\right)_{el} = K^0 (e^{(1-\alpha)\theta} a_{el} - e^{-\alpha\theta} b_{el}) \qquad (14)$$

$$\left(\frac{\partial a}{\partial N}\right)_{el} = -\frac{D_B}{D_A}\left(\frac{\partial b}{\partial N}\right)_{el} \qquad (15)$$

where α represents the transfer coefficient in this case.

Boundary conditions are then set in the R and Z directions as

$$\left(\frac{\partial a}{\partial R}\right)_{el} = \cos \alpha \left(\frac{\partial a}{\partial N}\right)_{el}; \left(\frac{\partial a}{\partial Z}\right)_{el} = \sin \alpha \left(\frac{\partial a}{\partial N}\right)_{el} \qquad (16)$$

$$\left(\frac{\partial a}{\partial R}\right)_{el} = -\frac{D_B}{D_A}\left(\frac{\partial b}{\partial R}\right)_{el}; \left(\frac{\partial a}{\partial Z}\right)_{el} = -\frac{D_B}{D_A}\left(\frac{\partial b}{\partial Z}\right)_{el} \qquad (17)$$

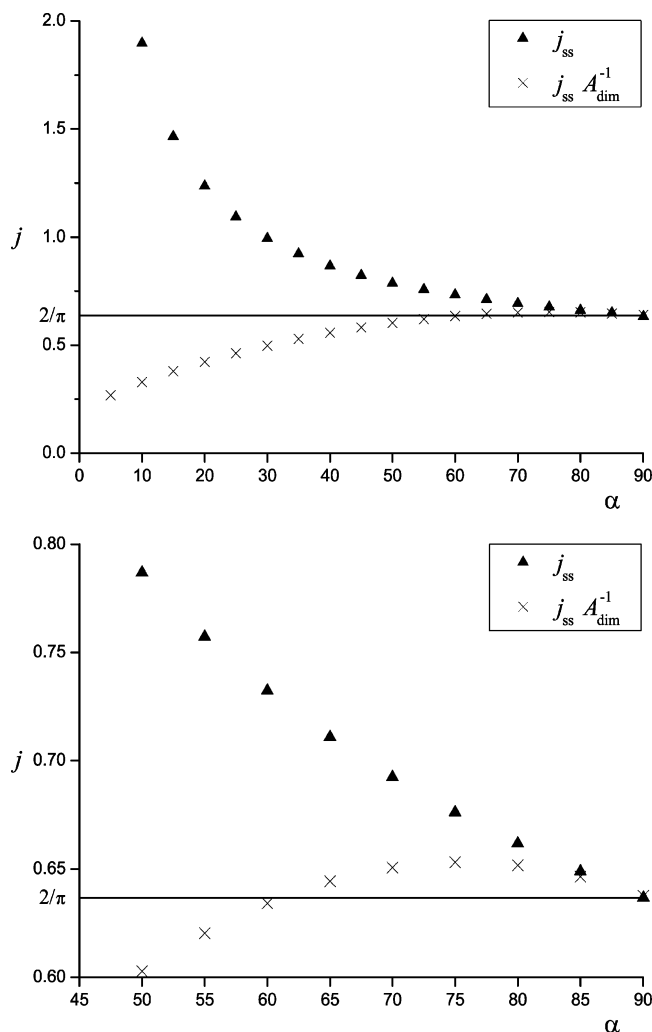Chronoamperometry, LSV, & CV at Various Electrodes

J. Phys. Chem. B, Vol. 112, No. 13, 2008 **4061**

Figure 4. Variation of j_{ss} and $j_{ss}A_{dim}^{-1}$ with α, with detail of region near the microdisc limit.

Figure 5. Concentration profiles at the steady-state mass transport limit: (a) $\alpha = 5°$; (b) $\alpha = 85°$.

The flux, similarly, is reported in the N direction as

$$\left(\frac{\partial a}{\partial N}\right)_{el} = \cos\alpha\left(\frac{\partial a}{\partial R}\right)_{el} + \sin\alpha\left(\frac{\partial a}{\partial Z}\right)_{el} \qquad (18)$$

This provides a local flux density, which is converted to dimensionless flux j by integrating across the surface area of the cone:

$$j = \sqrt{1 + \cot^2\alpha} \int_0^1 R\left(\frac{\partial a}{\partial N}\right)_{el} dR \qquad (19)$$

3. Mass-Transport Limited Currents

3.1. Analysis of Steady-State Current, j_{ss}. Steady-state currents, j_{ss}, in the mass-transport limit were assessed for cones of varying α from the $T \rightarrow \infty$ convergence of a system with the cone surface boundary condition $a_{el} = 0$. Simulation parameters were determined by increasing simulation accuracy until j_{ss} variation was <0.2%. The resulting current j_{ss} and current density $j_{ss}A_{dim}^{-1}$ vs α are shown at Figure 4, with the region 50° < α < 90° expanded for clarity in the following discussion. The microdisc value,[16] $j_{ss} = 2/\pi$, is shown for comparison.

Some deviations are noted from the values reported by Zoski et al.[8] for a similar system: for α < 70°, the literature data overestimates versus those reported here by approximately 1%, with substantial overestimates for α < 20°. We attribute this to
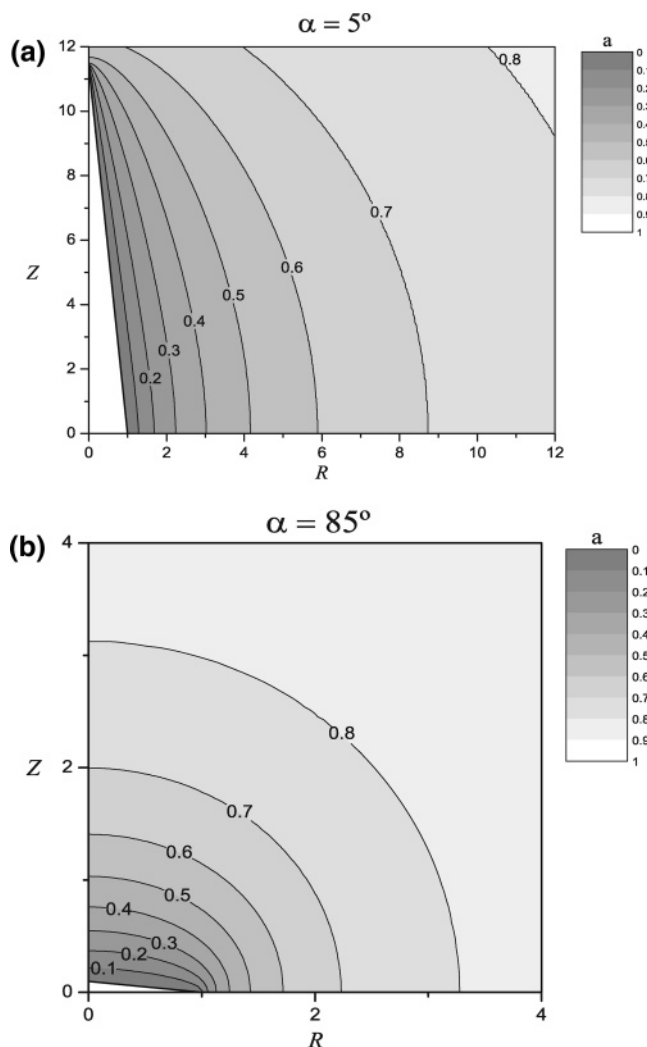
the less precise error tolerance and active suppression of grid density reported for these past simulations.

3.2. Rationalization of Trends in j_{ss} with Varying α. Trends in j_{ss} are best considered in terms of the current density, normalizing by A_{dim} in order to take full account of the increased area (and hence increased absolute current) of a cone as α is decreased at constant basal radius. The case $\alpha = 90°$ corresponds to a disc, and the expected limiting value of $j_{ss} = 2/\pi$ is observed as $\alpha \rightarrow 90°$. The case $\alpha = 0°$ is an infinite 1D plane along the Z axis, or equivalently, an infinite cylinder with $R_e = 0$. The limiting value $j_{ss} A_{dim}^{-1} = 0$ as $\alpha \rightarrow 0°$ is as expected, this being the $T \rightarrow \infty$ prediction of the Cottrell equation describing an infinite plane.

In each of these limiting cases, one site of nonplanar diffusion, the apex or the edge, becomes inactive; consequently, overall mass transport is reduced relative to a cone of intermediate α, in which both the apex and the edge increase steady-state current by acting as nonplanar diffusion sites. The concentration profiles shown in Figure 5 clearly demonstrate this. At $\alpha = 5°$, the concentration profile resembles that for a macroelectrode, but rotated along the Z axis, i.e., predominantly planar diffusion is observed with an imperceptible edge effect at $R = R_e$. At $\alpha = 85°$, however, the concentration profile closely resembles that for a microdisc, with no visible edge effect at $Z = Z_e$.

It is necessary to note, however, that the flux to a conical surface at the apex is not equivalent to flux at the edge, although
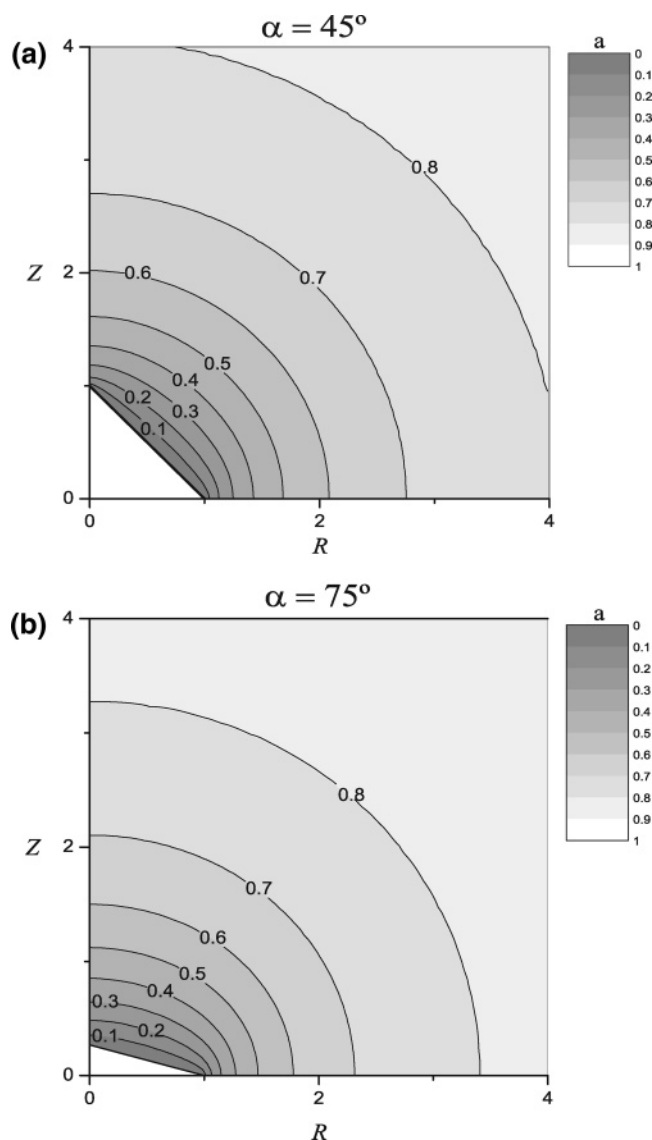
(a)

(b)

Figure 6. Concentration profiles at the steady-state mass transport limit: (a) $\alpha = 45°$; (b) $\alpha = 75°$.

it appears so in cross-section. Diffusion at the apex is much less significant than at the edge, because overall (3D) current response is R-dependent, and $R \rightarrow 0$ at the apex. Maximum current density for a conical electrode is not, then, achieved at $\alpha = 45°$, but rather close to $\alpha = 75°$ (Figure 4), as the importance of maximizing nonplanar diffusion at the edge greatly outweighs the importance of such maximization at the apex. The concentration profile for this case and that at $\alpha = 45°$ are shown at Figure 6.

3.3. Exploration of the Cottrellian Region for a Conical Electrode. At sufficiently short time scales following a potential step, the diffusion layer for an electrode does not extend far enough from the electroactive surface for its geometry, whatever it may be, to affect the chronoamperometric response. At short enough T, all electrodes then resemble an infinite planar system as described by the Cottrell equation: this system is characterized by the property $j \propto 1/\sqrt{t}$, a relation that does not hold at longer T for electrode geometries where convergent diffusion is possible. The extent of this Cottrellian region for conical electrodes of varying α was investigated by a simulation procedure similar to that above (Section 3.1), in this case using very short timesteps to accurately simulate the chronoamperometric transient immediately following a potential step.

The plot of log j vs log T presented at Figure 7 shows a Cottrellian straight-line region with a gradient of approximately $-1/2$ at $T < 10^{-2}$; beyond this, nonplanar diffusion causes significant deviation from the Cottrell equation for all values of α. This interpretation is confirmed by examination of a concentration profile at $T = 10^{-2}$ (Figure 8), in which the diffusion layer is seen to be largely planar, compared with those at the steady-state limit (Figure 6).

The extent of the Cottrellian region has important implications for voltammetry at conical electrodes. For a cone of $r_e = 0.5$ cm, the $T > 10^{-2}$ region is attained only at time scales longer than $t = 250$ s ≈ 4 min, for a typical value of D_A, so only planar, "macrocone" diffusion is observed on a voltammetric experimental time scale; for $r_e = 1$ μm, by contrast, the Cottrellian region is exceeded by $t = 10^{-5}$ s, so microelectrode behavior is expected. These analyses provide a useful starting point for direct simulation of linear sweep voltammetry at a conical electrode.

4. Voltammetry at an Isolated Cone

4.1. Theory of Simulating Voltammetry at an Isolated Cone. The general procedure described above (Section 2.2) is applied to linear sweep voltammetry (LSV) and cyclic voltammetry (CV) processes by linearly increasing or decreasing dimensionless potential θ in T by a dimensionless scan rate σ (see also Table 1):

$$\sigma = \left| \frac{\partial \theta}{\partial T} \right| \tag{20}$$

A Butler–Volmer boundary condition is applied as described above.

4.2. Effect of K^0 on the Voltammetric Response. In the electrochemically reversible limit, $K^0 \rightarrow \infty$, the results achieved are identical to those from a simple Nernstian boundary condition, i.e.,

$$\frac{a_{el}}{b_{el}} = e^{-\theta} \tag{21}$$

An exemplar voltammogram ($\alpha = 45°$) for $K^0 = 10^5$ vs Nernstian boundary conditions is shown in Figure 9. Trends as $K^0 \rightarrow 0$ are similar to those for other geometries: increased overpotential is required to drive electron transfer, and so j_{pf} occurs at $\theta \gg 0$ (see also Figure 9). Trends in j_{pf} as $K^0 \rightarrow 0$ are σ-dependent and are discussed below.

4.3. Effect of σ on the Voltammetric Response. High values of σ correspond to a "macrocone" limit. Either v, the dimensional scan rate, is very fast, or r_e is large. In either case, diffusion is slow on the experimental time scale, and so the diffusion layer achieved at the onset of diffusional control is largely planar and unaffected by the conical geometry, or by α. The forward peak current, j_{pf}, is then as predicted by the Randles–Ševčík equation[14] for a macroelectrode, with $A = A_{cone}$. In dimensionless parameters, this is

$$\text{Reversible } (K^0 \rightarrow \infty): \ j_{pf} = 0.223\sqrt{\sigma A_{dim}} \tag{22}$$

$$\text{Irreversible } (K^0 \rightarrow 0): \ j_{pf} = 0.248\sqrt{\sigma \alpha A_{dim}} \tag{23}$$

with α again representing the Butler–Volmer transfer coefficient in this case.

Low values of σ correspond, contrastingly, to a "microcone" limit. Either v is very slow, or, more realistically, r_e is small. Diffusion is accelerated on the experimental time scale, so a

Chronoamperometry, LSV, & CV at Various Electrodes

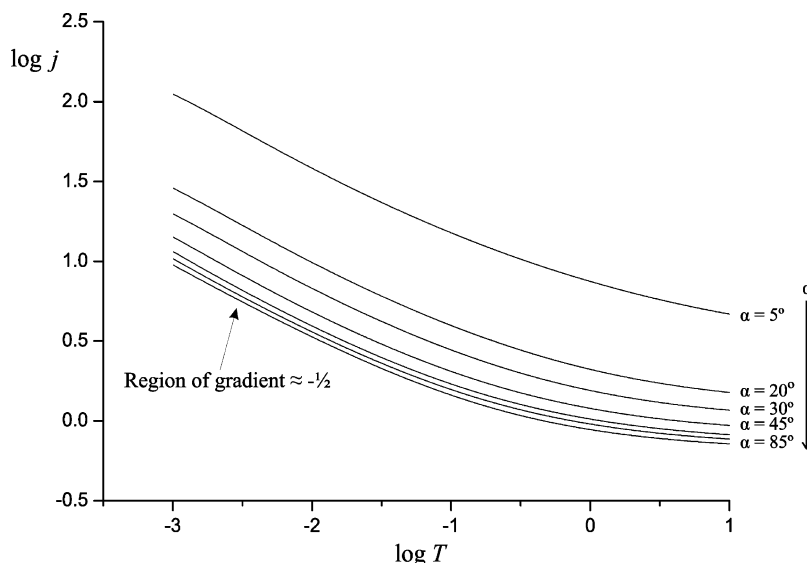*J. Phys. Chem. B, Vol. 112, No. 13, 2008* **4063**

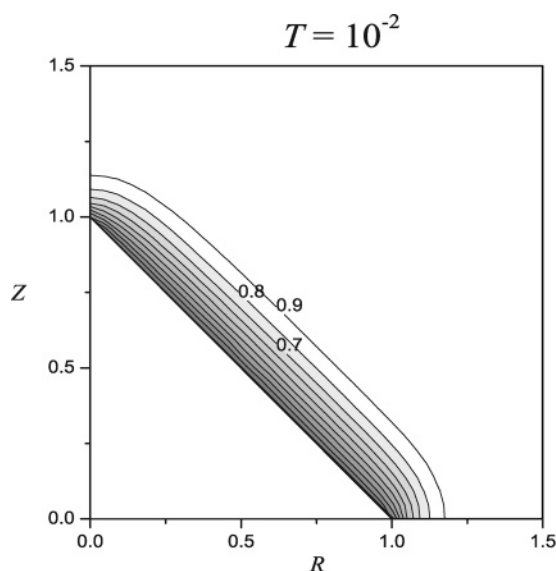**Figure 7.** Plot of $\log j$ vs $\log T$ for a chronoamperometric transient immediately following a potential step.

Figure 8. Concentration profile at $T = 10^{-2}$ following a potential step at a conical electrode, $\alpha = 45°$.
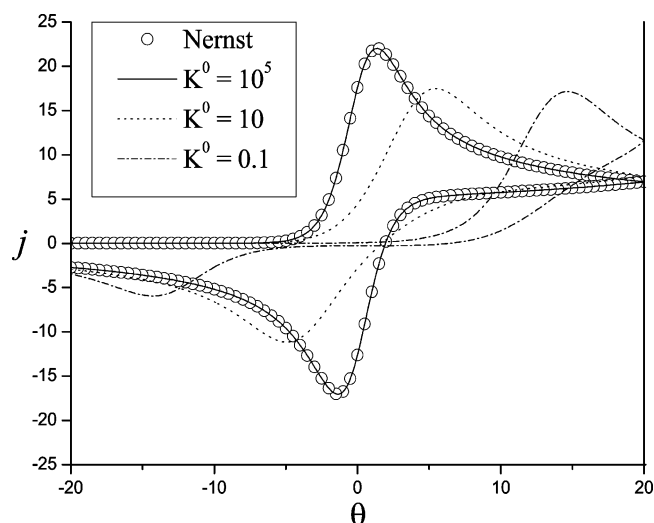

Figure 9. Simulated cyclic voltammograms at a conical macroelectrode ($\alpha = 45°$, $\sigma = 10^4$) for a Nernstian boundary condition and for Butler−Volmer boundary conditions at varying K^0.
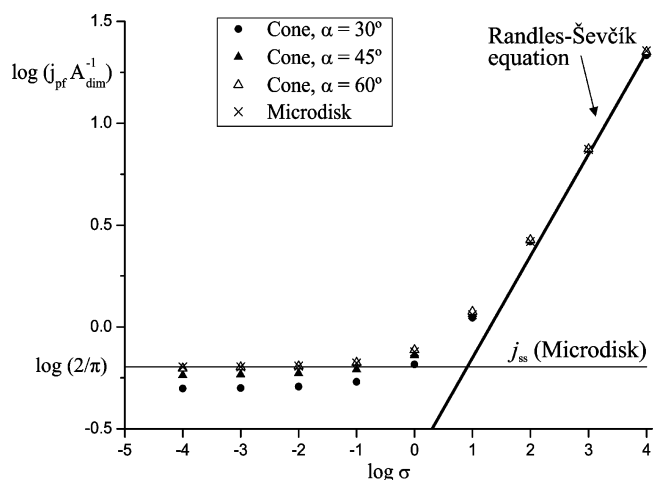

Figure 10. Plot of $\log j_{pf}$ vs $\log \sigma$ at varying α, showing convergence to both steady-state (Figure 4) and Randles−Ševčík behavior (eq 22).

near steady-state regime is achieved, with a substantially nonplanar diffusion layer where $\theta > 0$. j_{pf} greatly exceeds the values predicted by the Randles−Ševčík equation in this case, and approaches j_{ss} as $\sigma \rightarrow 0$. In this case, K^0 has no effect on j_{pf}, as the mass-transport limited current is rapidly achieved; K^0 simply affects the required overpotential to attain a diffusional limit.

Both cases are exemplified by voltammograms ($\alpha = 45°$) at Figure 9, and the overall trend is summarized by a plot of $\log(j_{pf} A_{dim}^{-1})$ vs $\log \sigma$, varying apex angle α in the Nernstian limit, in Figure 10. A plot of $\log(j_{pf}/j_{pf,Nernst})$ vs $\log K^0$ in Figure 11 summarizes the effect of K^0 for an exemplar system ($\alpha = 45°$).

4.4. Comparison to Voltammetry at a Conventional Microdisc. Trends with varying k^0 and σ are qualitatively identical to those for a microdisc. Nernstian and kinetically irreversible behaviors are equally well defined for a cone, and in the "macrocone" limit, the Randles−Ševčík equation is accurate. In this case, the apex angle α affects j_{pf} only indirectly by determining A_{dim} for the cone: variable geometry does not affect voltammetry where σ is large. Otherwise, nonuniformity of accessibility to the conical surface is important; observed

diffusion layers resemble those shown in Figure 6, with consequently similar trends relative to microdisc behavior as α is varied. The significance of nonplanar diffusion at the apex
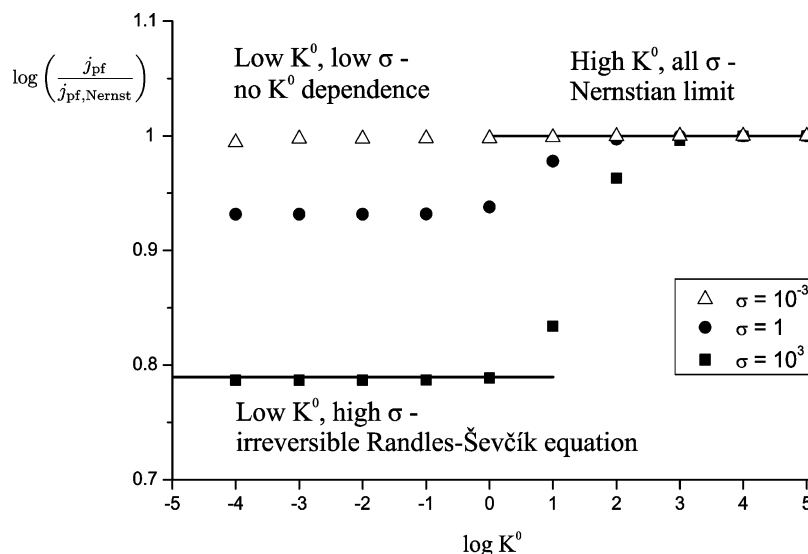
Figure 11. Plot of $\log j_{pf}$ vs $\log K^0$ at varying σ, showing convergence to irreversible Randles−Ševčík behavior (eq 23) for low K^0 and high σ, and no K^0 dependence for low σ.

of a conical electrode to its voltammetry is therefore limited to the low σ regime.

5. Regular and Random Arrays of Conical Electrodes

5.1. The Diffusion Domain Approximation. The diffusion domain approximation[9] is applied to model regular arrays of conical electrodes in a manner similar to that used by Davies et al. for regular arrays of microdiscs.[17] Each electrode in the array is treated as equivalent but diffusionally independent, and modeled in a cylindrical simulation space of area $A_{dim} = Ar_e^{-2} = d_{sep}^2$, where d_{sep} is the separation of electrodes in the array. If R_0 is the radial extent of the diffusion domain,

$$\pi R_0^2 = d_{sep}^2 \quad \text{so} \quad R_0 = \frac{d_{sep}}{\sqrt{\pi}} \tag{24}$$

At the boundary of the diffusion domain, $R = R_0$, a zero-flux boundary condition is set, implying equivalence with all neighboring domains:

$$R = R_0; \quad \left(\frac{\partial a}{\partial R}\right) = \left(\frac{\partial b}{\partial R}\right) = 0 \tag{25}$$

This boundary condition replaces the bulk boundary condition at $R = R_{max}$ used in simulations of isolated electrodes.

To extend this approach to a random array, it is necessary to consider that different electrodes will have differently sized diffusion domains. The random array is divided into Poisson−Voronoi cells,[18] each of which has some unique area s. Each cell is approximated to a diffusionally independent cylindrical domain of equivalent area, $A = s = \pi R_0^2$. Flux to a cylindrical diffusion domain is calculated for a wide range of R_0 values, and weighted according to the empirical frequency distribution of the Poisson−Voronoi cell area on a 2D surface:[18]

$$f(y) = \frac{343}{15}\sqrt{\frac{7}{2\pi}}\, y^{5/2}\exp\left(-\frac{7}{2}y\right) \tag{26}$$

where $y = s/\langle s \rangle$ and $s = \pi R_0^2$; $\langle s \rangle = \pi\langle R_0\rangle^2$, so

$$y = \left(\frac{R_0}{\langle R_0\rangle}\right)^2 \tag{27}$$

$\langle R_0\rangle$, the mean diffusion domain radius, corresponds to a characteristic electroactive surface coverage, Θ:

$$\Theta = \frac{\pi R_e^2}{\pi\langle R_0\rangle^2} = \frac{1}{\langle R_0\rangle^2} \tag{28}$$

For a regular array, it follows that

$$\Theta = \frac{\pi}{d_{sep}^2} \tag{29}$$

5.2. Results of Simulations at Arrays of Conical Electrodes. As with voltammetry at an isolated conical electrode (above), simulated voltammetry at arrays of conical electrodes is qualitatively very similar to that for microdiscs. The four behavioral cases for varying σ and Θ have been well defined by past work.[6] In the terminology introduced for arrays of microdiscs, Case 1 describes the limit where each electrode in the array has an individual planar diffusion layer, and the Randles−Ševčík current for an isolated electrode is observed. In Case 2, diffusion layers remain independent between electrodes, but diffusion layers are nonplanar, whereas, in Case 3, there is overlap between diffusion layers, with concomitant reduction in current. Case 4 describes the limit where diffusion layer overlap causes overall planar diffusion to the array surface, and so individual electrodes are not distinguishable, and a Randles−Ševčík current dependent on total array area is observed.

These cases are exhibited for conical electrode arrays ($\alpha = 45°$, $\sigma = 10^{-2}$) by the voltammetry in Figure 12. The expected equivalence between regular and random arrays for Cases 1 and 4 is demonstrated. In Cases 2 and 3, lower current is noted for the random array relative to that of the regular array (at equivalent Θ): this is consistent with past work on random arrays of electrodes, with various geometries.[7,17] The reduction in current is ≤30%, which also compares closely to other geometries. In the case pictured, it is ~20% at its most significant point.

Plots of $\log j_{pf}$ vs $\log \sigma$ for a regular array of conical electrodes (varying α, $\Theta = 0.04$) in the high and low σ limits are presented at Figure 13. It is clear that, at high σ (Case 1), j_{pf} tends to the Randles−Ševčík result for an isolated conical

Chronoamperometry, LSV, & CV at Various Electrodes
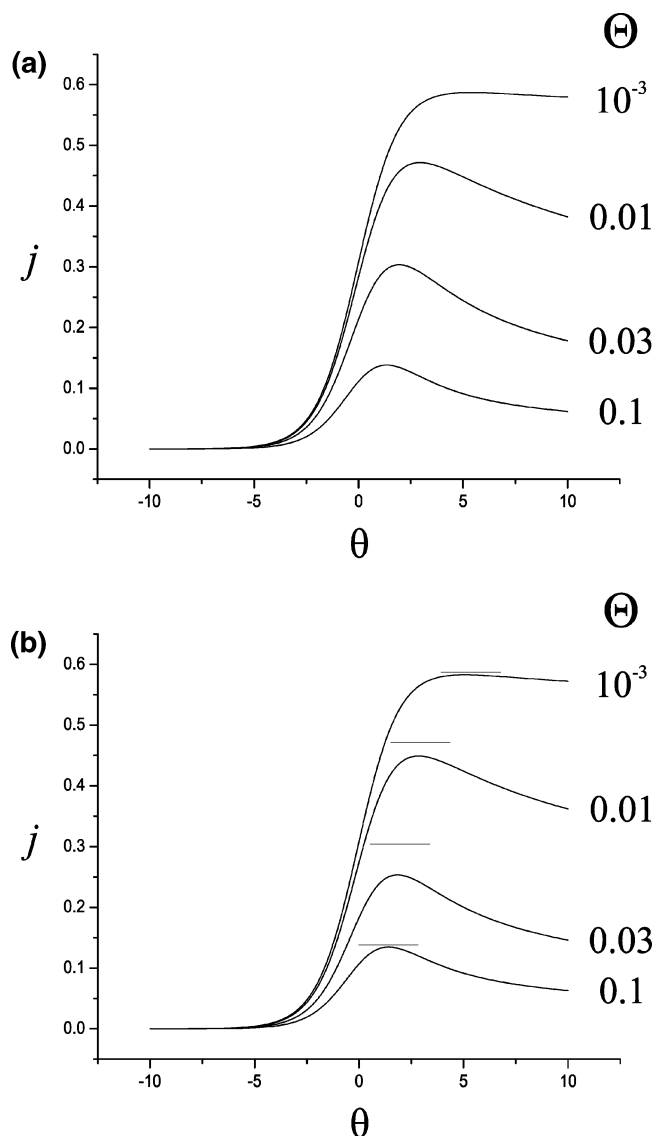
J. Phys. Chem. B, Vol. 112, No. 13, 2008 **4065**

Figure 12. Comparative cyclic voltammetry for arrays of conical electrodes, with $\sigma = 10^{-2}$, $\alpha = 45°$ and varying electroactive surface coverage Θ: (a) A regular array; (b) a random array showing regular array currents (—) for comparison.

electrode (eq 22), and, at low σ (Case 4), j_{pf} tends to the Randles−Ševčík result for a plane of $A = \pi\langle R_0\rangle^2$, irrespective of α. For an isolated electrode, by contrast, j_{pf} tends to j_{ss} in this limit.

In all realistic cases, the Z extent of the diffusion layer near the Case 4 limit is much greater than cot α, and so the dimensions of the cone do not visibly affect the value of σ at which the Case 4 limit is achieved; similarly, Case 1 behavior is defined by a diffusion layer occurring only very close to the surface, so α affects j_{pf} close to this limit only by determining A_{dim}, as discussed for the isolated cone above (Section 4.4).

The Case 2 to 3 transition is shown in detail in Figure 14. Here $\log(j_{pf} A_{dim}^{-1})$ vs $\log \sigma$ is plotted for both a regular array of conical electrodes (varying α, $\Theta = 0.04$) and an isolated electrode. The enhanced j_{ss} reported above (Section 3.2) from $\alpha = 30°$ to $\alpha = 60°$ was rationalized on the basis of increased edge effects at $R = R_e$. These edge effects increase the thickness of the diffusion layer in the R direction, so diffusion layer overlap is expected to occur at higher σ for $\alpha = 60°$ than for lower α. From analysis of the data produced, it appears that this is indeed the case, although the difference is small, and
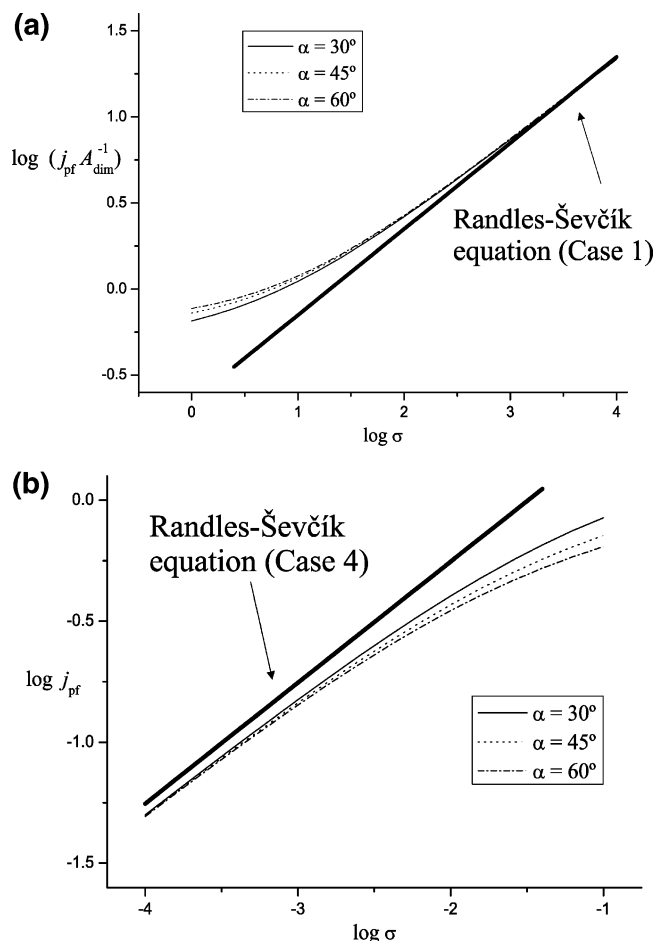

Figure 13. Plot of $\log j_{pf}$ vs $\log \sigma$ for a regular array of conical electrodes ($\Theta = 0.04$) at varying α, showing convergence to Randles− Ševčík behavior in (a) Case 1 and (b) Case 4.
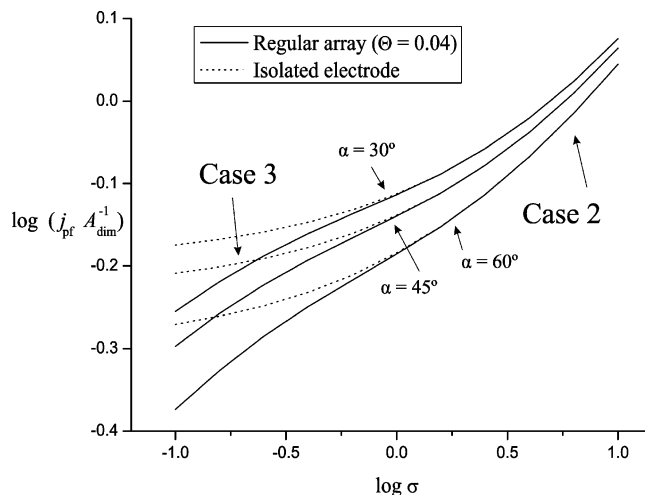

Figure 14. Plot of $\log(j_{pf} A_{dim}^{-1})$ vs $\log \sigma$ for a regular array of conical electrodes ($\Theta = 0.04$) at varying α, showing the Case 2 to 3 transition.

cannot be seen in Figure 14. Defining the transition as occurring at $j_{pf,Array}/j_{pf,isol} < 0.99$, it occurs at $1 < \sigma < 1.5$ for all α shown.

Very similar behavior for all cases is observed for a random array, with the exception of reduced current response for Cases 2 and 3, as noted above. A plot of $\log(j_{pf} A_{dim}^{-1})$ vs $\log \sigma$ for a random array of conical electrodes ($\alpha = 45°$, $\Theta = 0.04$) is shown in Figure 15, with the trend for an isolated electrode also plotted for comparison.
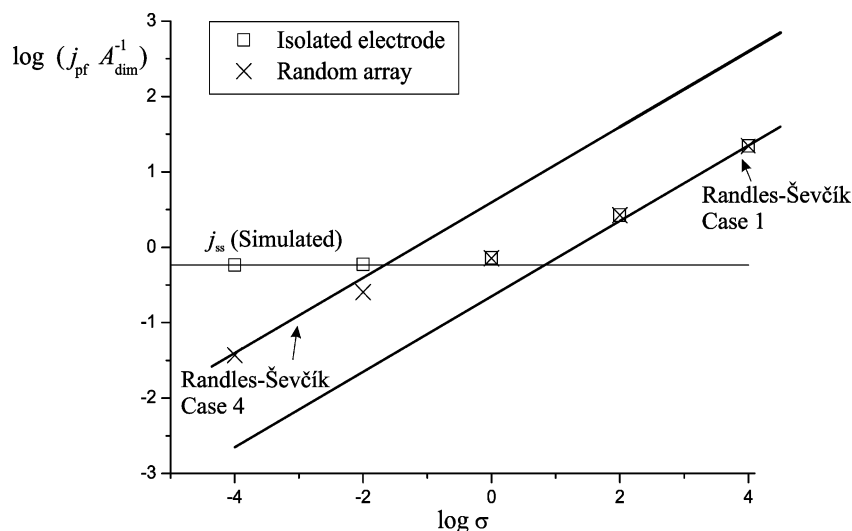
Figure 15. Plot of $\log(j_{pf} A_{dim}^{-1})$ vs $\log \sigma$ for a random array of conical electrodes ($\alpha = 45°$, $\Theta = 0.04$) and an isolated conical electrode, showing Case 1 to 4 behavior for the array and divergent behavior from an isolated electrode at low σ.

6. Conclusions

In this work, the current response at an electroactive conical surface has been considered under both chronoamperometric (potential step) and voltammetric (potential sweep) conditions. Trends have been rationalized in terms of the apex angle α, the fundamental parameter describing the shape of the cone. Section 3.2 demonstrated that tall cones behave like rotated planar electrodes, and flat cones behave like microdiscs; in the intermediate region, nonplanar diffusion at both the edge and apex of the cone were found to enhance diffusion-limited current. We have additionally shown that the cyclic voltammetry of conical electrodes is qualitatively similar to that at a microdisc, both for isolated electrodes and for arrays. The four behavioral cases known for regular and random arrays of microdiscs[6] were replicated.

We have successfully adapted known numerical techniques for microdiscs[12] to a more complicated geometrical situation. This then invites further study of nonuniformly accessible electrodes, especially those with two edge sites, e.g., cylinders, or those closely related to this work, e.g., recessed cones. The development of the conical system to consider multiple electron transfers and coupled homogeneous kinetics is also proposed as a route of future research.

References and Notes

(1) Cai, Y.; Ocko, B. M. *J. Am. Chem. Soc.* **2005**, *127*, 16287−16291.

(2) Li, T.; Zhang, X.; Jiang, X.; Li, Y.; Du, Z. *Chin. Sci. Bull.* **2005**, *50*, 2560−2564.

(3) Diegoli, S.; Hamlett, C. A.; Leigh, S. J.; Mendes, P. M.; Preece, J. A. *J. Aerosp. Eng.* **2007**, *221*, 589−629.

(4) Lemay, S. G.; van den Broek, D. M.; Storm, A. J.; Krapf, D.; Smeets, R. M. M.; Heering, H. A.; Dekker, C. *Anal. Chem.* **2005**, *77*, 1911−1915.

(5) Yokoo, A. *J. Vac. Sci. Technol.* **2003**, *21*, 2966−2969.

(6) Davies, T. J.; Banks, C. E.; Compton, R. G. *J. Solid State Electrochem.* **2005**, *9*, 797−808.

(7) Streeter, I.; Compton, R. G. *J. Phys. Chem. C* **2007**, *111*, 15053−15058.

(8) Zoski, C. G.; Mirkin, M. V. *Anal. Chem.* **2002**, *74*, 1986−1992.

(9) Amatore, C.; Savéant, J.-M.; Tessier, D. *J. Electroanal. Chem.* **1983**, *147*, 39−51.

(10) Peaceman, J. W.; Rachford, H. H. *J. Soc. Ind. Appl. Math.* **1955**, *3*, 28−41.

(11) Atkinson, K. E. *Elementary Numerical Analysis*, 3rd ed.; John Wiley and Sons: New York, 2004.

(12) Gavaghan, D. J. *J. Electroanal. Chem.* **1998**, *456*, 1−24.

(13) Britz, D.; Strutwolf, J. *Electrochim. Acta* **2006**, *52*, 33−41.

(14) Bard, A. J.; Faulkner, L. R. *Electrochemical Methods, Fundamentals and Applications*, 2nd ed.; John Wiley and Sons: New York, 2001.

(15) Gavaghan, D. J. *J. Electroanal. Chem.* **1997**, *420*, 147−158.

(16) Saito, Y. *Rev. Polarogr.* **1968**, *15* (6), 177−187.

(17) Davies, T. J.; Compton, R. G. *J. Electroanal. Chem.* **2005**, *585* (1), 63−82.

(18) Járai-Szabó, F.; Néda, Z. *Physica A (Amsterdam)* **2007**, *385* (2), 518−526.